This article has been accepted for publication in IEEE Open Journal of Ultrasonics, Ferroelectrics, and Frequency Control. This is the author's version which has not been fully edited and content may change prior to final publication. Citation information: DOI 10.1109/OJUFFC.2024.3371913

Received XX Month, XXXX; revised XX Month, XXXX; accepted XX Month, XXXX; Date of publication XX Month, XXXX; date of current version XX Month, XXXX.

Studying the Effects of Mutual Acoustic Impedance on the Performance of Polymer-Based CMUTs

MARTIN ANGERER[1, 2], JONAS WELSCH[1], CARLOS D. GERARDO[1], NICOLE V. RUITER[2], EDMOND CRETU[1], AND ROBERT ROHLING[1]

[1]Department of Electrical and Computer Engineering, The University of British Columbia, Vancouver, Canada
[2]Institute for Data Processing and Electronics, Karlsruhe Institute of Technology, Karlsruhe, Germany

CORRESPONDING AUTHOR: Martin Angerer (e-mail: m.angerer@ubc.ca).

ABSTRACT

The objective of this work was to investigate changes in the acoustic characteristics of micromachined transducers caused by acoustic cross-coupling between cells. We used hexagonal, polymer-based capacitive micromachined ultrasonic transducers (polyCMUTs) consisting of 127 cells connected in parallel. The distances between the cells were varied, while the cell dimensions and number of cells remained constant. The resulting changes in characteristics were evaluated in terms of peak frequency f_{pk}, fractional bandwidth FBW, peak transmit sensitivity S_{pk} and opening angle Φ_t. The study relies on results from an analytic multicell model (MCM) which considers cross-coupling effects between cells through a mutual acoustic impedance matrix. The results are compared with finite element (FE) analyses and measurements on fabricated prototypes. The manufacturing processes used to produce the polyCMUT prototypes are explained in detail. We found significant changes in all acoustic characteristics: as cell spacing increases, f_{pk} and Φ_t decrease, while S_{pk} gradually rises to about twice the initial value. The FBW varies due to the change in f_{pk}, peaking at small to intermediate cell-to-cell distances. While both modeling approaches cover the general effects, discrepancies in comparison to the measurements were identified. The FE model provided better fits than the analytic MCM, albeit at significantly higher computational costs. The effects on the acoustic characteristics were found strongest at lower frequencies and if many cells are in close proximity to each other. Hence, rotational symmetric or square transducers operating at lower frequencies are affected most. The results demonstrate that design approaches based on modeling single cells may lead to significant deviations from design goals. Both, analytic and FE models are suitable tools to estimate the effects of acoustic interactions and to predict the performance. This aids in meeting design requirements of micromachined ultrasound transducers consisting of multiple radiators.

INDEX TERMS acoustic cross-coupling, polymer-based CMUTs, mutual acoustic impedance, analytic multicell model, microfabrication process, 2-D transducer arrays, ultrasound tomography

I. INTRODUCTION

ULTRASOUND imaging systems require the generation of well-defined acoustic fields to unfold their imaging potential. The design of ultrasound transducers was therefore optimized over decades to match the needs of a variety of imaging setups and systems [1–4]. New imaging approaches require transducer technologies to facilitate a large design freedom, cost-effective production and excellent acoustic performance. With the commonly used piezoelectric transducers, these requirements can be hard to achieve [5, 6].

Capacitive Micromachined Ultrasonic Transducer (CMUTs) offer a larger design freedom, possibility for high-volume production and superior ultrasound performance [7–9]. This led to investigations in almost all applications, where piezoelectric transducers are currently being used [10]. In CMUTs, the ultrasound is generated by the movement of thin membranes, driven by electrostatic forces. These membranes are typically manufactured by micromachining silicon layers, leveraging the advantages from semiconductor manufacturing [11].

The working frequency range of a single circular CMUT is defined by the thickness and diameter of the membrane. In order to reach the diagnostic ultrasound frequency range (ca. 0.5 to 16 MHz), diameters smaller than 100 μm are typically

This work is licensed under a Creative Commons Attribution 4.0 License. For more information, see https://creativecommons.org/licenses/by/4.0/

This work is licensed under a Creative Commons Attribution-NonCommercial-NoDerivatives 4.0 License. For more information, see https://creativecommons.org/licenses/by-nc-nd/4.0/

This article has been accepted for publication in IEEE Open Journal of Ultrasonics, Ferroelectrics, and Frequency Control. This is the author's version which has not been fully edited and content may change prior to final publication. Citation information: DOI 10.1109/OJUFFC.2024.3371913

required [12]. This results in low transmit sound pressures due to the small active area. Hence, finalized transducers (or also called elements in arrays) usually consist of multiple CMUT cells connected in parallel. The macroscopic acoustic field results from the superposition of the radiation behavior of these cells.

If multiple sound radiators are driven in close proximity at the same time, the performance of one of these radiators might be affected by all the others [13]. In order to predict the macroscopic acoustic field accurately, an understanding of the acoustic interactions in terms of self- and mutual impedances is required. Porter [14] developed an analytic formalism to predict the acoustic interactions between flexural disk radiators, giving an applicable theory for CMUTs. The presented expressions depend only on the wave number k, the radius a of the radiators and the distance d between them.

A variety of studies were conducted to better understand these acoustic effects and their impact on the design of CMUT elements. Caronti et. al [15] conducted the first comprehensive study of multiple CMUT cells via finite element (FE) analyses. This study found that mutual acoustic impedance effects are a major source of cross-coupling in CMUTs if the cells are packed closely together ($d << \lambda_0$, here λ_0 is the wavelength). This cross-coupling has an effect on the macroscopic acoustic characteristics, leading to a reduced bandwidth with increasing cell spacing [16]. Senlik et. al [17] extended these findings using a combination of FE analyses and analytic formulations. They predicted the radiation resistance of an element when varying the cell-to-cell distances. A maximum in radiation resistance and thus, an optimum in acoustic transmission power was found at a distance of 1.25 λ_0. However, this would result in very large cell diameters and oversized elements, leading to challenges in fabrication and inept array designs.

An analytic model for predicting the acoustic field of a CMUT element was presented by Oguz et. al [18]. Porters exact equation [14] was approximated for a limited range of cell radii ($ka < 5.5$) using a tenth order polynomial to facilitate calculations. A very good fit between the analytic model and FE analysis was achieved. Maadi et al. [19] extended this approach to cells with different cell radii, giving a comprehensive modeling framework for multi-frequency arrays.

More recently, Merrien et. al [20] presented a method to model elements of linear arrays with a single two-port network model. Their approach is based on reducing the degree of freedom of a CMUT element, consisting of multiple cell-columns, to a single piston transducer. This is possible when considering the element's aspect ratio [21] and periodic radiation boundary conditions. The resulting model enables very fast solving and quick design analysis, but its applicability is limited to linear arrays and uniform cell-to-cell spacing. For applicable designs, a methodology is presented to meet the targeted center frequency.

The aforementioned studies showed strong effects on the acoustic field depending on the number of cells, the cell arrangement and the cell-to-cell distance. Hence, to accurately meet specific transducer requirements, these effects have to be considered in the CMUT element design process. In previous work, we presented the analysis of hexagonal elements consisting of 127 cells using a FE model [22]. A good fit between measurement and model was achieved in terms of acoustic performance. However, the large number of design parameters and cells result in FE models with many million degrees of freedom. This makes FE analysis impractical.

The primary goal of this study was to explore acoustic cross-coupling between cells and its practical implications on the acoustic performance of transducers composed of multiple radiators. Our approach is based on increasing the cell-to-cell distances in an element, while keeping the number of cells constant. This ensures a constant active area (surfaces of the cell membranes). Changes in the acoustic field are studied using two different modeling approaches and measurements on fabricated prototypes. Differences are discussed and recommendations are given to optimize element designs for specific applications.

Increasing the cell-to-cell distances leads to larger elements, and consequently, to changes in the acoustic field and a more focused beams. We evaluated the emitted sound pressure in the far-field for all element sizes to mitigate focusing effects on the frequency responses. Changes in directivity are assessed by evaluating the acoustic field over a large range of emission angles. This study was motivated by optimizing the transmission performance of polymer-based CMUTs (polyCMUTs) for 3-D ultrasound applications. Hence, the developed designs encompass rotational symmetric elements, derived from the requirements of 3-D ultrasound tomography [6, 22, 23].

This study is divided into three sections: In the first section, the two modeling approaches are introduced. The first encompasses an analytic multi-cell model (MCM), derived from literature. The MCM uses the equivalent circuit method, and is valid for arbitrary element shapes, number of cells and cell positions within the element. A focus is laid on predicting the acoustic far-field. The second model encompasses a 3-D FE analysis of entire elements and full coupling of the required physics.

In the second section, the design and production of prototype transducers is presented. These prototypes were fabricated using a novel process to manufacture CMUTs using polymer layers instead of silicon [24]. These polymer layers are deposited on silicon wafers to form the vibrating membranes. The fabrication processes are presented in detail, leading to functional polyCMUT prototypes for characterization.

In the third section, results from the models are compared with measurements. The effects of the increase in cell-to-cell distance with respect to the acoustic field are identified and

This work is licensed under a Creative Commons Attribution-NonCommercial-NoDerivatives 4.0 License. For more information, see https://creativecommons.org/licenses/by-nc-nd/4.0/

tracked. Hypotheses on the change in acoustic characteristics are formulated and design recommendations for specific applications are given.

II. MODELING METHODS

Given the extensive design parameter space of polyCMUTs, employing an analytic model allows for the rapid analysis of design variations and parameter combinations. However, the generation of ultrasound with CMUTs involves the vibration of microscopic structures, different physics domains and nonlinear deformations. This requires approximations, which might lead to a limited prediction accuracy [15]. To address this, we decided to additionally model the transducers using the FE method. A FE model facilitates precise representations of the microscopic geometric features, and permits the consideration of non-linear effects. This can provide additional insights into the technology and allows for validation of the analytic model though at significantly higher computational costs.

This manuscript focuses on the description and evaluation of the analytic model, described in the following sections. A in-depth description of the implemented FE models can be found in [22]. In a nutshell, the FE model was implemented in COMSOL v6.1 (Comsol Inc, Stockholm, Sweden) and incorporates full coupling of Structural Mechanics, Electrostatics and Pressure Acoustics physics. This enables accurate predictions of the acoustic fields. The polyCMUT elements were modeled in 3-D, resulting in up to 1.2 million mesh elements and more than 3 million degrees-of-freedom. The models were solved using a computing cluster to facilitate computation.

A. ACOUSTIC FIELD CHARACTERISTICS

Before introducing the analytic MCM, more explanations on the referred transducer characteristics are given. Ultrasonic transducers generate a specific acoustic field, defined by the transducer technology, shape, embedding and utilized amplifiers. The acoustic field can be displayed as diffraction field pattern, giving the transmitted sound pressure depending on the incident angle and frequency. This depiction of transducer performance enables the derivation of typical figures of merit used to compare different designs and technologies. Fig. 1 shows the modeled diffraction field pattern of an exemplary piezoelectric piston transducer. This transducer is based on a PZT fiber with 0.46 mm diameter and 0.6 mm length. The performance is predicted using a 2-D piston model and a circular aperture [25]. Detailed information on this example can be found in [26, Ch. 6].

Four transducer characteristics will be used throughout this manuscript for comparison and evaluation. These encompass the peak frequency f_{pk}, fractional bandwidth FBW, opening angle Φ_t and peak transmit sensitivity S_{pk}, indicated in Fig. 1. FBW equals f_{pk}/bw, where bw is the frequency range within a -6 dB drop in sound pressure at 0° emission angle. Φ_t is obtained at 2 MHz and a signal drop of -10 dB. These characteristics enable the comparison of different designs with scalars within a constant measurement distance and a given frequency range.

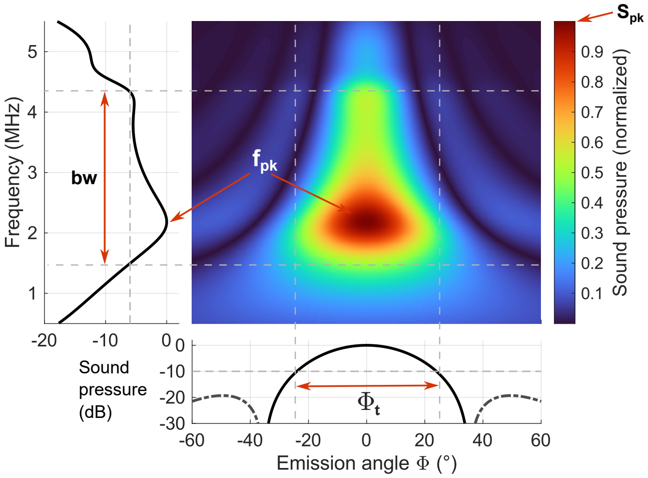

FIGURE 1. Modeled diffraction field pattern of a piezoelectric piston transducer in the far-field to obtain the acoustic characteristics f_{pk}, bw, Φ_t and S_{pk}.

B. ANALYTIC MULTICELL MODEL

To analytically predict the diffraction field pattern of transducers consisting of multiple radiators, we used an equivalent circuit model. This enables rapid solving, easy adjustments (e.g. adding parasitics) and direct integration with readout circuits. The equivalent circuit model is illustrated in Fig. 2. It can be divided into three steps or sections: First, the electro-acoustic conversion of each cell is represented through a transformer and a few lumped electrical components. Second, the acoustic interactions between cells are modeled with a radiation impedance matrix. Third, the macroscopic acoustic field is predicted by summing the emissions from all radiators.

The electro-acoustic conversion of each cell follows Mason's equivalent circuit model [27]. The electrical capacitance of the transducer is modeled with C_0, and the input voltage is converted to a force by a transformer with ratio n. The spring softening effect is considered via $-C_0/n^2$ [28], transferred to the secondary side of the transformer. Z_m depicts the complex mechanical impedance of the membrane. The derivation and calculation of C_0 and n is well described in literature [29–31], and is not subject of this work.

To model acoustic interactions between the cells, we followed the formalism presented by Oguz et. al [18]. The cells are acoustically connected by the complex impedance matrix $\mathbf{Z_a}$. This matrix depends on the number of cells, the cell radius a, the center-to-center distance d between the cells and the frequency. The acoustic pressure field is finally calculated using the Rayleigh integral. In summary, the equivalent circuit model relies on the following assumptions and defined boundary conditions:

This work is licensed under a Creative Commons Attribution-NonCommercial-NoDerivatives 4.0 License. For more information, see https://creativecommons.org/licenses/by-nc-nd/4.0/

This article has been accepted for publication in IEEE Open Journal of Ultrasonics, Ferroelectrics, and Frequency Control. This is the author's version which has not been fully edited and content may change prior to final publication. Citation information: DOI 10.1109/OJUFFC.2024.3371913

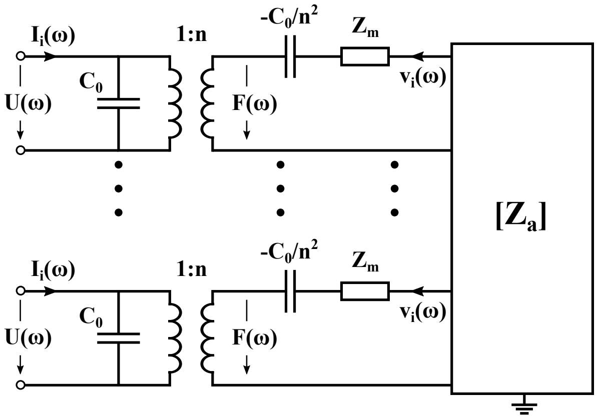

FIGURE 2. **ECM of a polyCMUT element. Each cell is modeled as individual resonator. $\mathbf{Z_a}$ acoustically couples all cells considering self- and mutual radiation impedance.**

- The transducer is assumed to be a linear system, meaning that it's response is proportional to the input signal.
- The model is only valid for the lowest-order vibration mode of the membranes.
- The membranes are modeled as laminates with multiple non-zero layers.
- The membranes are assumed to be clamped radiators to obtain their mechanical impedance Z_m.
- All material properties are assumed to be isotropic and uniform.
- All cells are excited in parallel without phase shifts between the cells.
- All cells in the element are of equal diameter.
- The cells are located on an infinite rigid plane baffle.
- For estimating the directivity, each element is assumed to be a clamped edge piston radiator with a uniform surface.
- The diffraction field pattern is calculated at a fixed radial distance in the far-field.

More detailed explanations on these assumptions and how the model was derived are given in the following sections. The model is solved at discrete frequencies using MATLAB v9.12 (Mathworks, MA, USA). This programming environment enables fast adaptations, efficient computation and direct access to powerful post processing capabilities.

C. SINGLE CELL MODEL

Each polyCMUT cell is modeled with the aforementioned four lumped electrical components. Since the membrane consists of multiple layers, calculating the mechanical impedance Z_m requires equivalent laminate parameters. To obtain these, we followed the procedure described in [32]. The flexural rigidity D_l of a laminate is given in (1), where $E(m)$ is the Young's modulus, and $\nu(m)$ the in-plane Poisson's ratio of the m-th layer. $\bar{h}(m)$ is the distance from the top of the respective layer to the neutral axis.

$$D_l = \frac{1}{3}\sum_{m=1}^{M}\frac{E(m)}{1-\nu(m)^2}(\bar{h}(m)^3 - \bar{h}(m-1)^3) \qquad (1)$$

For circular membranes with no residual stress, Z_m can be obtained according to (2) [29]. There, ω is the angular frequency, J_1 the first-kind Bessel function of first order and I_1 the modified Bessel function of first order, respectively. ρ_l and t_l are the density and thickness of the laminate.

$$Z_m(\omega) = \frac{j\omega\rho_l t_l K(\omega)}{K(\omega) - 4\mathrm{J}_1(k_m a)\cdot \mathrm{I}_1(k_m a)} \qquad (2)$$

with

$$\begin{aligned} K(\omega) = k_m a[&\mathrm{J}_0(k_m a)\cdot \mathrm{I}_1(k_m a) \\ &+\mathrm{J}_1(k_m a)\cdot \mathrm{I}_0(k_m a)] \end{aligned} \qquad (3)$$

The wave number k_m of the laminate is given in (4). It is calculated from the equivalent parameters of the laminate and varies with frequency.

$$k_m(\omega) = \sqrt[4]{\frac{\omega^2 \rho_l t_l}{D_l}} \qquad (4)$$

D. ACOUSTIC COUPLING

This section briefly introduces the formalism used to consider the acoustic coupling between the cells and the medium in order to obtain the coupling matrix $\mathbf{Z_a}$. More theory and detailed explanations can be found in [14] and [18]. For a given pair of cells in an element, the total acoustic impedance of one cell can be expressed as

$$Z_1(\omega) = Z_{11}(\omega) + \frac{v_2(\omega)}{v_1(\omega)} Z_{12}(\omega), \qquad (5)$$

where Z_{11} is the self radiation impedance, v_1 and v_2 the rms velocity of each cell membrane, and Z_{12} is the mutual acoustic impedance between the radiators. Greenspan [33] gave the following analytic expression to calculate Z_{11} of a clamped circular radiator:

$$\begin{aligned} F_1(y) &= (20-y^2)\mathrm{J}_1(y) - 7y\mathrm{J}_0(y) - 3y \\ F_2(y) &= (y^2-20)\mathrm{H}_1(y) + 7y\mathrm{H}_0(y) - 2y^2/3\pi \\ Z_{11}(\omega) &= \rho c S(1-192/y^5)\cdot[F_1(y) + jF_2(y)]. \end{aligned} \qquad (6)$$

In this expression, $y = 2ka$, where $k = \omega/c$ is the acoustic wave number and a the radius of the cell. ρ and c are the density and speed-of-sound of the medium, and S is the surface area of the cell. H_0 and H_1 are Struve functions of first and second order, respectively.

Oguz et. al [18] approximated Z_{12} with the expression given in (7), where d_{12} is the center-to-center distance of the cells. $A(ka)$ is a function fitted to the exact solution using a tenth order polynomial and is valid for $ka < 5.5$.

$$Z_{12}(\omega) \simeq \rho c S \cdot A(ka)\frac{\sin(kd_{12}) + j\cos(kd_{12})}{kd_{12}} \qquad (7)$$

This work is licensed under a Creative Commons Attribution-NonCommercial-NoDerivatives 4.0 License. For more information, see https://creativecommons.org/licenses/by-nc-nd/4.0/

This article has been accepted for publication in IEEE Open Journal of Ultrasonics, Ferroelectrics, and Frequency Control. This is the author's version which has not been fully edited and content may change prior to final publication. Citation information: DOI 10.1109/OJUFFC.2024.3371913

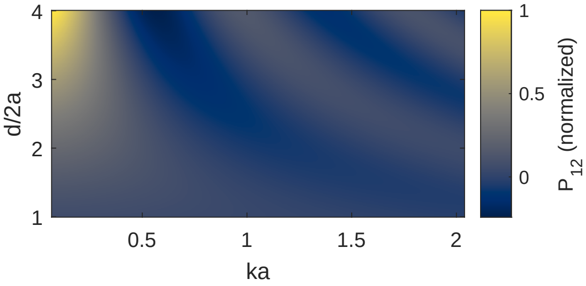

FIGURE 3. **Example of the effective mutual radiation power of two cells with radii of 40 µm over a given frequency and cell-to-cell distance range.**

Z_{12} is a complex impedance and describes how the radiation of the two cells depend on the frequency, cell diameter and the center-to-center distance. From this impedance, the effective mutual radiation power P_{12} can be calculated, assuming a unity force excitation:

$$P_{12}(\omega) = \Re(\frac{1}{Z_{12}(\omega)}). \tag{8}$$

An example how P_{12} changes with frequency and cell-to-cell distance is given in Fig. 3. In this example, a is 40 µm and the frequency ranges from 0.4 to 12 MHz, resulting in the shown values for ka. The distances between the cells were varied from $2a$ to $8a$. The results suggests that the effective output power added from mutual impedance effects increases with the cell-to-cell distance for frequencies up to 0.4 ka. The maximum can be found at low frequencies and very large cell-to-cell distances. For higher frequencies, intermediate distances result in a larger power. Interesting are the ranges where P_{12} becomes negative. This would reduce the effective acoustic emission and should be avoided in a design.

The formalism presented for two cells can be extended to an arbitrary number of cells. This results in the acoustic coupling matrix

$$\mathbf{Z_a}(\omega) = \begin{bmatrix} Z_{11}(\omega) & Z_{21}(\omega) & \cdots & Z_{N1}(\omega) \\ Z_{12}(\omega) & Z_{22}(\omega) & \cdots & Z_{N2}(\omega) \\ \vdots & \vdots & \ddots & \vdots \\ Z_{1N}(\omega) & Z_{2N}(\omega) & \cdots & Z_{NN}(\omega) \end{bmatrix}, \tag{9}$$

where N is the total number of cells in the array. $\mathbf{Z_a}$ is by definition a square matrix whose size increases with the number of cells. For elements with hundreds of cells, this leads to very large matrices. However, the dimensions can be significantly reduced when considering the acoustical reciprocity theorem ($Z_{ij} = Z_{ji}$). Moreover, if all radiators are identical, the self radiation impedance is the same, leading to a symmetric matrix.

E. ACOUSTIC FIELD CALCULATION

Before estimating the macroscopic acoustic field, the model from Fig. 2 needs to be solved. The acoustic force acting on the surrounding medium is given with

$$F(\omega) = \mathbf{Z}(\omega) \cdot v(\omega), \tag{10}$$

where $\mathbf{Z}$ is the acoustic impedance and v the rms velocity [34]. Since all lumped acoustic circuit components are connected in series, $\mathbf{Z}$ results in:

$$\mathbf{Z}(\omega) = (\frac{jn^2}{\omega C_0} + Z_m(\omega)) \begin{bmatrix} 1 & 0 & \cdots & 0 \\ 0 & 1 & \cdots & 0 \\ \vdots & \vdots & \ddots & \vdots \\ 0 & 0 & \cdots & 1 \end{bmatrix} + \mathbf{Z_a}(\omega). \tag{11}$$

The velocity of each cell can then be calculated using (12), which requires the inversion of $\mathbf{Z}$. The input voltage $U(\omega)$ is transformed to an acoustic force by the ratio n.

$$v_i(\omega) = \mathbf{Z}(\omega)^{-\mathbf{1}} \cdot \frac{n}{U(\omega)} \tag{12}$$

From the velocity of each cell, the generated macroscopic far-field pressure can be calculated by the Rayleigh integral

$$p(r, \Phi, \omega) = j\frac{\rho c k S}{2\pi} \cdot D(\Phi, \omega) \cdot \sum_{i=1}^{N} v_i(\omega) \cdot \frac{e^{-jkr_i}}{r_i}, \tag{13}$$

where r_i is the radial distance of the i-th cell to the observation point [18]. D gives the directivity of a clamped piston radiator [14] with

$$D(\Phi, \omega) = 48\frac{\mathrm{J}_3(ka\sin(\Phi))}{ka\sin(\Phi)^3}. \tag{14}$$

The approximation of the diffraction field with (13) enables a very fast estimation of the acoustic far-field. However, some errors are introduced since the actual acoustic aperture is not a closed surface but consists of multiple small radiators driven in parallel.

III. PROTOTYPE TRANSDUCERS

For the purpose of this study, we developed several polyCMUT prototypes. This allows for validating the developed models and to get quantitative data on mutual acoustic impedance effects when the cell-to-cell distances increase. This section presents the design, fabrication, integration and testing of the realized prototypes.

A. DESIGN

Using polymer layers to fabricate CMUTs is a novel and interesting approach since it addresses several disadvantages of silicon-based CMUTs. Some advantages of polyCMUTs are reduced fabrication costs, rapid prototyping capability and the possibility to fabricate fully-flexible transducer arrays [35]. Moreover, the microfabrication process of polymer layers omits the need for toxic solvents and allows for lower pull-in voltages due to the reduced stiffness of the laminate [24]. At the University of British Columbia (UBC), we developed a process to reliably fabricate polyCMUTs [24]. The basic structure of a polyCMUT cell is shown in the

This work is licensed under a Creative Commons Attribution-NonCommercial-NoDerivatives 4.0 License. For more information, see https://creativecommons.org/licenses/by-nc-nd/4.0/

This article has been accepted for publication in IEEE Open Journal of Ultrasonics, Ferroelectrics, and Frequency Control. This is the author's version which has not been fully edited and content may change prior to final publication. Citation information: DOI 10.1109/OJUFFC.2024.3371913

TABLE 1. **Layer definition and thicknesses of the prototype elements.**

Layer	Material	Thickness
Bottom electrode	Ti/Au	5/50 nm
Insulation	Ti/SiO_2	5/60 nm
First polymer	SU-8	540 nm
Top electrode	Ti/Au	5/50 nm
Second polymer	SU-8	2400 nm
Passivation	Parylene-C	4000 nm
Membrane thickness	*Laminate*	*6995 nm*

TABLE 2. **Material parameters used for the analytic MCM and FE analyses.**

Material	ρ	E	ν	ϵ_r
Au	19300 kg/m^3	70 GPa	0.44	3.2
SiO_2	2200 kg/m^3	70 GPa	0.17	4.2
SU-8	1218 kg/m^3	5.9 GPa	0.33	3.2
Parylene-C	1249 kg/m^3	2.8 GPa	0.40	-

cross section in Fig. 5. The membrane consists of several polymer layers, while the deposited metal layers enable the application of an electric field.

For this study, we chose a circular cell design due to the available experience in terms of reliable fabrication at UBC and to achieve isotropic emission characteristics [36, Ch. 7]. The peak frequency of a single cell was aimed at around 2 MHz. The cavity radius was set to 40 µm. This results in the layer thicknesses given in Table 1. We chose an element design with 127 cells to ensure sufficient output pressure, while keeping the overall dimensions of the element small. This results in larger Φ_t.

The cells in the element are arranged in a honeycomb pattern to ensure a constant cell-to-cell distance. Four designs with the following distances were chosen: 88 µm, 132 µm, 176 µm and 220 µm. The first distance is the feasible minimum for the technology, given the chosen cell diameter of 80 µm. The other three distances are multiples of half the first, covering a kd range of 0.7 to 1.9 at 2 MHz.

The resulting shape of the elements is hexagonal, giving a quasi-isotropic acoustic field in azimuth and elevation. The resulting cell arrangement for the 88 µm and the 220 µm element are shown in Fig. 4. The increased cell-to-cell distance results in a significantly larger outer dimension of the element. The number of cells was kept constant. The material parameters used for the models are given in Table 2.

B. FABRICATION

We fabricated the polyCMUTs used in this study via a process based on the work of Gerardo et. al [24] and Welsch et. al [37]. However, there were several changes to account for recent improvements of the polyCMUT fabrication process. The microfabrication flow only uses two distinct processes to create the seven layers needed: thin-film metal deposition, patterning and liftoff as well as polymer patterning and development. All processes are additive, meaning that no silicon-based material etching takes place. This removes the need for highly concentrated and highly toxic chemicals. Fig. 5 gives an overview of the fabrication process and the involved process steps.

First, a four-inch silicon wafer coated with 500 nm thermal oxide was used as a substrate. To create the pattern for the bottom electrode, the wafer is coated with nLOF 2020 (Merck Performance Materials GmbH, Germany) via a spin coating process at 3000 rpm for 30 s. The resist is soft-baked at 110°C for 1 min with no ramp. It is then exposed via a 350 nm laser at a dose of 110 mJ/cm^2 in a maskless lithography system (MLA 150, Heidelberg Instruments, Germany). After exposure, the resist is hard-baked for 1 min at 110°C. After cooldown, the pattern is developed in AZ 300 MIF (Merck Performance Materials GmbH, Germany), a low concentration Tetramethylammonium Hydroxide (TMAH) based developer, for 70 s and quenched in deionised (DI) water. In the next step, the patterned wafer is transferred into an electron beam physical vapor deposition machine (AJA UHV Hybrid Evaporator System, A JA International, MA, USA) where 5 nm Titanium (Ti) and 50 nm Gold (Au) are deposited. The Ti layer acts as an adhesion layer, avoiding delamination of the bottom electrode from the Silicon Dioxide (SiO_2) substrate. After deposition, the photoresist is removed through an Acetone bath and the wafer is cleaned with DI water and dehydrated on a hotplate.

This process is repeated with a deposition of 5 nm Titanium and 60 nm of SiO_2 using the aforementioned electron beam deposition machine. The Ti again acts as an adhesion promoter while the SiO_2 is intended as an electric insulation layer. This avoids short circuits due to the low breakdown voltage of the thin SU-8 layer should the membrane collapse. Because this is an additive process, the insulation layer is slightly thicker with its outlines overlapping the bottom electrodes by 5 µm to aid further spin coatings and improve adhesion.

In the next process step, the sacrificial layer is patterned via a two-layer liftoff process. LOR 3A (Kayaku Advanced Materials, MA, USA) is spin coated at 3000 rpm for 30 s and hard-baked at 180°C. After cooldown, the wafer is then coated with Microposit S1813 (Shipley Company, MA,

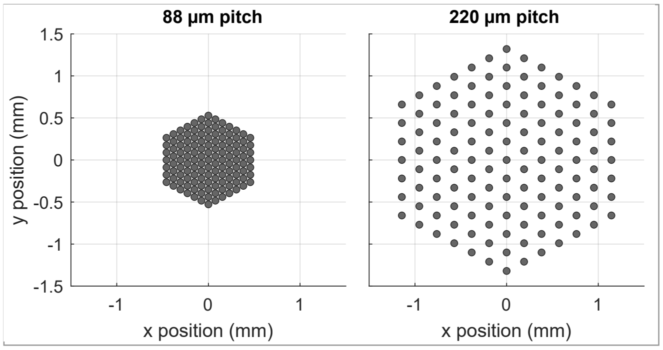

FIGURE 4. **Hexagonal element designs with the smallest (left) and largest (right) cell-to-cell distance used in this study.**

This work is licensed under a Creative Commons Attribution-NonCommercial-NoDerivatives 4.0 License. For more information, see https://creativecommons.org/licenses/by-nc-nd/4.0/

This article has been accepted for publication in IEEE Open Journal of Ultrasonics, Ferroelectrics, and Frequency Control. This is the author's version which has not been fully edited and content may change prior to final publication. Citation information: DOI 10.1109/OJUFFC.2024.3371913

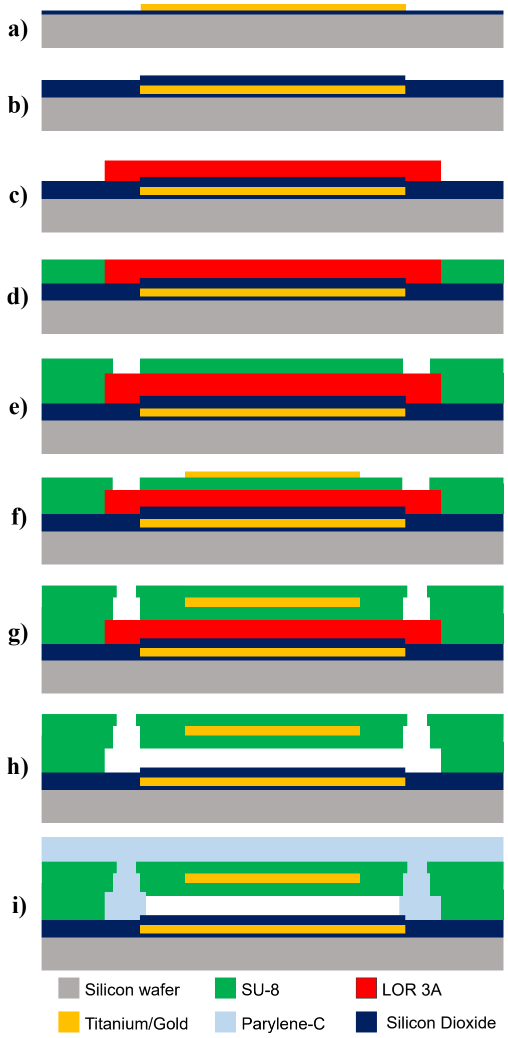

FIGURE 5. **Overview of the used polyCMUT fabrication processes for a single cell (from [37]): a) Silicon wafer with insulation and deposited bottom electrode; b) Deposition of insulation layer; c) Deposition of sacrificial layer; d) Added base layer; e) Patterned first membrane layer; f) Deposition of top electrode; g) Patterned second membrane layer; h) Etching of the cavity and membrane release; i) Sealing and conformal coating.**

USA) to create a masking layer. This is necessary due to the photo insensitivity of LOR 3A. The resist is soft-baked at 110°C and exposed in the MLA 150 at 285 mJ/cm^2. After exposure, the layer is developed for 60 s in AZ 300 MIF. The S1813 is then washed away in an Acetone bath.

The next layer, called the SU-8 base layer, is needed to even-out the topology of the fabricated layers (see [37]). Because the following first membrane layer should be as thin as possible, the areas between the sacrificial layer structures need to be filled with slightly higher or at least the same height as all previous layers stacked on top (roughly 320 nm). To aid adhesion and structural stability, the layer is fabricated from SU-8 2000.5 (Kayaku Advanced Materials, MA, USA). If spin coated at high enough speeds (>4000 rpm) a layer thickness of less than 500 nm can be reached. After spin coating, the resist is soft-baked at 95°C for 3 min, exposed for 8 s in a physical mask aligner (NxQ 4006, Neutronix Quintel, CA, USA), post-exposure baked for 1 min at 95°C and developed in SU-8 Developer (Kayaku Advanced Materials, MA, USA) for 1 min. Following is a 5 min hard-bake at 150°C. This process is repeated for the first membrane layer. After another deposition of 5 nm Ti and 50 nm Au as the top electrode via the aforementioned process, the second membrane layer is patterned. The same process is used as for the subsequent SU-8 layers, with the only difference being a post-exposure bake time of 2 min and a development time of 1.5 min with the resist being SU-8 2002 (Kayaku Advanced Materials, MA, USA). All resulting layer thicknesses are listed in Tab. 1.

When all layers have been patterned, the wafer is diced with a dicing saw (Disco DAD3204, Disco Corporation, Japan) and the resulting chips are placed in AZ 300 MIF to etch the LOR sacrificial layer. When all residues of LOR have been removed, the chips are placed in 2-Propanol (IPA) to displace the etchant. The chips are then placed in a critical point dryer (Autosamdri-815B, Tousimis, MD, USA) in order to obtain released membranes. A microscope image of a fabricated transducer is shown in Fig. 6a).

C. INTEGRATION AND TESTING

After releasing the membranes, the samples are mounted on custom printed circuit boards (PCBs) and electrically connected with conductive adhesive (EpoTek EJ2189-LV, Epoxy Technology, MA, USA). The entire PCB is then covered with a 4 µm layer of Parylene-C (SCS Labcoater 2, Speciality Coating Systems, IN, USA). The low-pressure conformal coating process also seals the membrane cavities by filling the existing vertical etch holes. An additional protection and insulation layer for the electrical bonds was foreseen with UV-curable adhesive (OG-116, Epoxy Technology, MA, USA).

The PCBs were finally integrated in a cylindrical housing and sealed with adhesive (BondIt B-45, Reltek, CA, USA) to avoid water leakage. A finalized prototype is shown in Fig. 6c). The entire fabrication process can be completed in one week, entirely in our local clean room. This highlights the potential for rapid prototyping of the polyCMUT technology.

To assess the general functionality of the fabricated devices, we measured the electrical input impedance with an impedance analyzer (HP 4294A, Keysight, CA, USA). A comparison between four samples with different cell-to-cell distances and the by the MCM predicted electrical impedance is shown in Fig. 6b). The MCM predicts the resonance frequency in air at 3.6 MHz, while the measurements reside slightly higher. An offset in impedance is present, arising from a higher parasitic capacitance than anticipated (approx. 8 pF). Since material damping is currently not considered in the MCM, a sharper peak in phase angle is present. The mean electromechanical coupling factor k_t^2 was

This work is licensed under a Creative Commons Attribution-NonCommercial-NoDerivatives 4.0 License. For more information, see https://creativecommons.org/licenses/by-nc-nd/4.0/

This article has been accepted for publication in IEEE Open Journal of Ultrasonics, Ferroelectrics, and Frequency Control. This is the author's version which has not been fully edited and content may change prior to final publication. Citation information: DOI 10.1109/OJUFFC.2024.3371913

found to be 0.13. It was calculated according to 15, where C_{LF} is the low-frequency capacitance, and C_{HF} is the high-frequency capacitance of the transducers [38].

$$k_t^2 = 1 - \frac{C_{HF}}{C_{LF}} \tag{15}$$

For acoustic characterization, we measured the diffraction field pattern within a 120-degree circular segment at a radial distance of 4 cm. We used a relatively low DC bias of 40 V to prevent shorts caused by the limited breakdown voltage of SU-8 (approx. 112 V/µm). The transmitted ultrasound was captured using a needle hydrophone (Onda HNC-0400, Onda, CA, USA), installed on an automated XYZ-stage within a water tank as depicted in Fig. 6d). To assess the broadband characteristics, the transducers were excited with a linear chirp signal with frequencies ranging from 0.5 to 7 MHz. Subsequently, the recorded ultrasound signal underwent normalization and bandpass filtering to yield the transmit sensitivity in Pascal per Volt.

When testing the produced samples, we faced challenges in reliability and variations in performance. We excluded samples which significantly deviated from the predictions to rule out effects arising from fabrication (e.g. only partial release of the membranes). Those samples used for testing showed a stable and repeatable performance over the testing period (1-2 months).

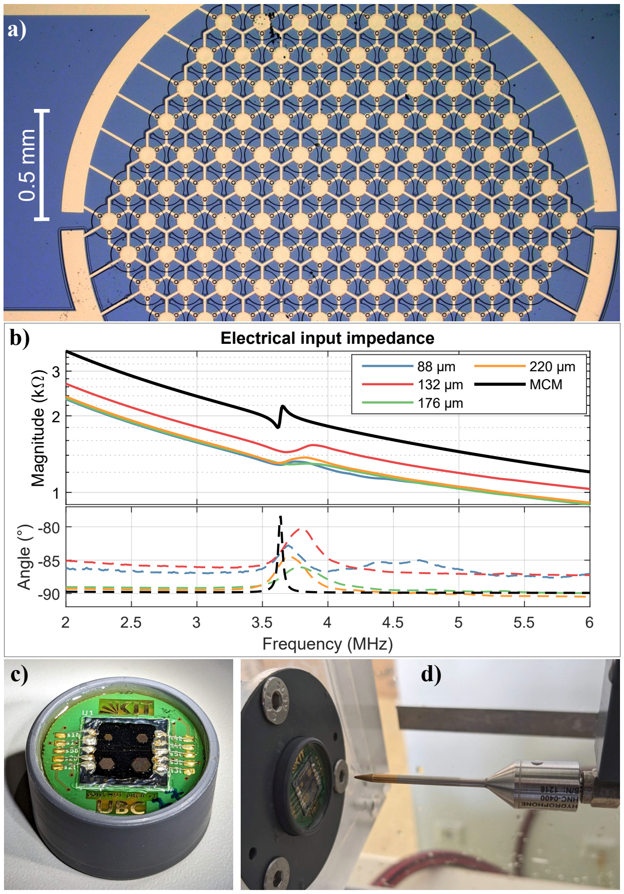

FIGURE 6. PolyCMUT transducers. (a) Image of a fabricated element with 176 µm cell-to-cell distance. (b) Comparison of the electrical input impedance between four measurements and predictions by the MCM at 40 V DC bias. (c) Assembled prototype with all four designs on one chip. (d) Hydrophone measurement setup to characterize the acoustic field.

IV. RESULTS

In this section, we compare the results from the analytic MCM and the FE model with measurements performed on the fabricated prototypes. But first, we want to give a comparison in terms of computation between the two models. Table 3 lists the computational effort and environments used for solving. Almost five times more increments were studied with the analytic MCM in only a fraction of the time. This highlights the potential of the analytic approach to study a broad range of parameters.

A direct comparison of the diffraction field pattern between results from the analytic MCM, the FE analysis and one exemplary measurement is shown in Fig. 7a) and b). The results for the smallest (88 µm) and the largest (220 µm) are depicted. The analytic MCM predicts the general pattern in terms of directivity, sound pressure and frequency range well. Interesting are the predicted and measured pressure fluctuations below 2 MHz for the 88 µm samples. These fluctuations likely arise from dispersive Rayleigh-Bloch waves, forming additional resonances within these wavelengths [39].

The axial transmit sensitivity of all four investigated cell-to-cell distances are shown in Fig. 7c). Both, the analytic MCM and the FE model predict a significant change in resonance behavior with increasing cell distances. While the general behavior is well predicted with the analytic MCM, the results from the FE model match the measurements better. As the distance between cells increases, the resonance peak becomes more pronounced. Similar effects were observed by Boulme et. al [21], stating a direct decrease in bandwidth when increasing the cell-to-cell distance. Based on the shown results, the following effects can be hypothesized:

- f_{pk} shifts to lower frequencies with increasing cell-to-cell distances.
- The FBW changes as expected with f_{pk}, but decreases with increasing cell-to-cell distances.
- S_{pk} rises with increasing cell-to-cell distances.

In order to get a better overview of the impact of these effects, the changes in acoustic characteristics with increasing cell-to-cell distances are shown in Fig. 8. The results

TABLE 3. Comparison between the analytic MCM and the FE model in terms of computational costs. The "Dist." column gives the number of different cell-to-cell distances that were examined using the models.

Model	Dist.	Station	Resources	Time
Analytic MCM	64	Local computer	12 cores (4.1 GHz), 32 GB RAM	0 h, 3 min and 37 s
FE Model	13	Computing cluster	64 cores, 84 GB average memory	25 h, 35 min and 13 s

This work is licensed under a Creative Commons Attribution-NonCommercial-NoDerivatives 4.0 License. For more information, see https://creativecommons.org/licenses/by-nc-nd/4.0/

from the analytic MCM, which takes advantage of its low computational costs, are represented by a continuous curve. The results of 13 distinct FE analyses and the measurements at the four investigated distances are shown with the markers.

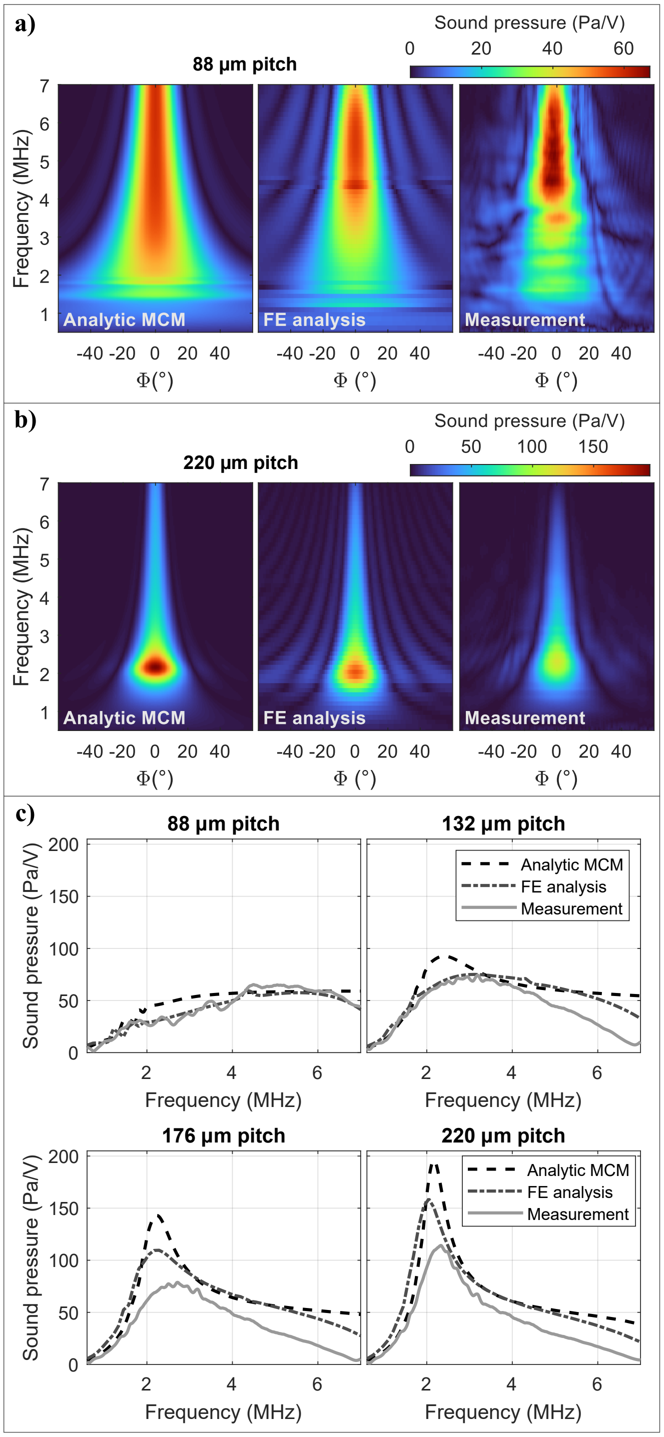

FIGURE 7. **Comparing the results from the analytic MCM, the FE analysis and exemplary measurements on the produced prototypes. (a) Diffraction field pattern at a cell-to-cell distance of 88 µm and (b), a cell-to-cell distance of 220 µm, both at 4 cm radial distance. (c) Transmitted sound pressure over frequency in water at $\Phi = 0^\circ$ and 4 cm axial distance for all four investigated cell-to-cell distances.**

The hypothesized changes in acoustic characteristics are better depicted in these graphs. f_{pk} decreases with increasing cell-to-cell distances from initially above 5 MHz down to 2 MHz. The latter value matches the predicted resonance peak of a single cell. S_{pk} substantially increases, though the measured rise is not as substantial as predicted with the models. The reduction in Φ_t is attributed to the larger area of the element, narrowing down the transmitted beam.

Interesting are the changes in FBW. In general, a variation can be expected since the fractional bandwidth depends on f_{pk}. However, the analytic MCM predicts a defined maximum at a pitch of 147 µm, with a substantial decrease afterwards. Based on the more sparse data from the FE simulations, this maximum is shifted towards larger distances at around 165 µm. The measured characteristics follow this trend, but with less prominent variations. Important to notice is that the frequency range was limited to a maximum of 7 MHz, motivated by the requirements from 3-D ultrasound tomography and to limit the size of the FE models. This ensures comparability of all generated results but leads to lower FBW values in case f_{pk} is close to the upper frequency limit. A quantitative comparison of the acoustic characteristics at the four investigated cell-to-cell distances is given in Table 4.

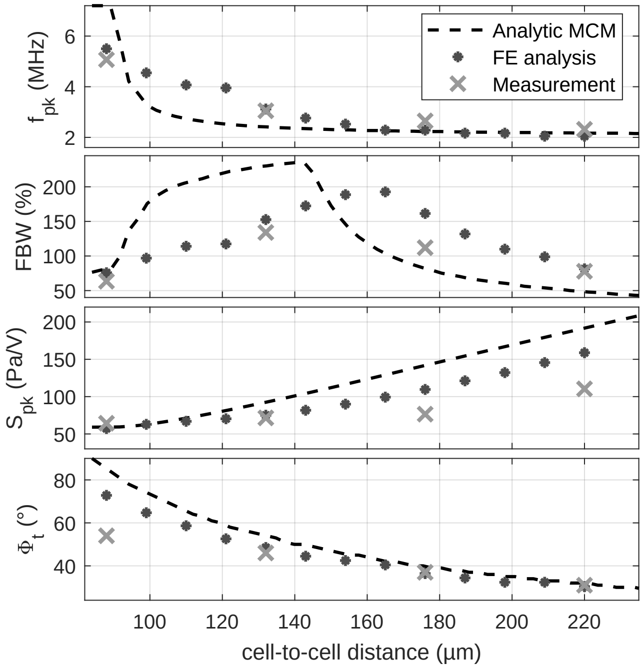

FIGURE 8. **Changes in acoustic characteristics when varying the cell-to-cell distances in the shown rage. The cells have a diameter of 80 µm. The results from FE simulations and four measurements are shown with the markers. The dashed line arises from the analytic MCM and was computed based on 64 simulations with equidistant increments. The FBW was calculated up to a maximum frequency of 7 MHz.**

This work is licensed under a Creative Commons Attribution-NonCommercial-NoDerivatives 4.0 License. For more information, see https://creativecommons.org/licenses/by-nc-nd/4.0/

This article has been accepted for publication in IEEE Open Journal of Ultrasonics, Ferroelectrics, and Frequency Control. This is the author's version which has not been fully edited and content may change prior to final publication. Citation information: DOI 10.1109/OJUFFC.2024.3371913

TABLE 4. Comparison of acoustic characteristics between the analytic MCM, the FE analyses and measurement for the four investigated cell-to-cell distances.

Distance	Modality	$\mathbf{f_{pk}}$ (MHz)	FBW (%) (-6 dB)	$\mathbf{S_{pk}}$ (Pa/V)	$\mathbf{\Phi_t}$ (°) (-10 dB)
88 µm	An. MCM	7.0	80	59	89
	FEA	5.5	76	57	72
	Meas.	5.1	64	64	54
132 µm	An. MCM	2.4	230	92	54
	FEA	3.1	153	75	49
	Meas.	3.1	134	71	46
176 µm	An. MCM	2.2	83	141	40
	FEA	2.3	161	110	36
	Meas.	2.7	112	78	37
220 µm	An. MCM	2.2	48	193	32
	FEA	2.1	75	158	30
	Meas.	2.3	78	122	31

V. DISCUSSION

We found significant changes of the acoustic field when increasing the cell-to-cell distances of polyCMUT elements. The investigated elements consist of 127 cells in an hexagonal arrangement, with a cell diameter of 80 µm. The cell-to-cell distance varied from 88 to 220 µm. The effects were studied with both, an analytic MCM and FE model. The predicted effects are then compared with measurements. A key finding is that the peak frequency in water for a single cell varies significantly from the peak frequency when multiple cells are in close proximity. For the investigated designs, the modeled and measured f_{pk} exceeds 5.1 MHz, while that of a single cells is at around 2 MHz. This difference decreases with increased cell spacing. Similar effects were reported in literature, where a shift in center frequency and a reduction in bandwidth was predicted when increasing the cell-to-cell distance in an element (see [40], [16] and [20]).

Along with the changes in f_{pk}, Φ_t also decreases while S_{pk} gradually increases. The results also suggest that there is an optimal pitch to maximize FBW for the investigated design within the used frequency range. The analytic MCM predicts this spot at 1.7 times the diameter of the cells, while the FE analyses suggest slightly larger distances. However, this optimal pitch is not fully representative since the frequency range was limited to 7 MHz to keep the FE simulations feasible. Hence, the results are only valid for the investigated cell design, cell arrangement and frequency range.

The optimal pitch arises predominately from the shift in f_{pk} towards lower frequencies. Parameter studies using the analytic MCM showed that this pitch depends on the utilized frequency range and coupling medium. Two examples are illustrated in Fig. 9a), where the upper frequency limit is increased from 7 MHz to 12 MHz, and the acoustic medium is changed from water to IPA. Shifting the upper frequency limit prevents a cut-off in bandwidth, while IPA exhibits a lower acoustic impedance (0.92 MRayl compared to 1.5 MRayl of water). In both cases, the maximum in FBW shifts towards smaller cell-to-cell distances, indicating that the cells need to be densely packed to achieve a large bandwidth. The predicted FBW exceeding 300% seems implausible and is unlikely to be observed in a real-life design.

The increase in cell-to-cell distances causes a substantial enlargement of the elements, which impacts the acoustic field. Hence, it is important to ascertain whether the findings may result, at least partially, from varying the total radiation surface. To investigate this, we conducted simulations utilizing the analytic MCM, wherein the cell-to-cell distances increased while the outer dimensions of the elements remained constant. This leads to a gradual reduction in cells and consequently the active area. The results of this simulation study are shown in Fig. 9b). $\mathbf{\Phi_t}$ was neglected since the outer dimensions of the elements remained constant. The progression of f_{pk} and FBW is relatively similar to the results from Fig. 8. This suggests that mutual acoustic impedance effects are the primary cause of the presented findings. The step-wise decrease in S_{pk} results from the reduction in active area. Within a constant number of cells, however, a gradual increase can be observed.

The results from this additional study demonstrate that the radiated sound pressure per transducer area decreases as the distances between the cells increase. In case of ultrasound application where the surface area is limited, increasing the cell spacing might not be a prudent option. A careful review of the cell geometry is then required to still reach the aimed acoustic characteristics. The design rules given by Merrien et. al [20] give a guideline for linear arrays in this regard.

When space and beam focusing is not a limiting factor, a trade-off between peak sensitivity and bandwidth can be achieved for different cell-to-cell distances. Focused ultrasound (FUS) applications come into mind since the utilized transducers are typically driven with low-bandwidth tone bursts and require strong focusing [41]. Choosing larger cell-to-cell distances could increase the peak pressure, leading to more efficient FUS transducers.

The effects of acoustic cross-coupling on the acoustic field appear to be strongest for larger wavelengths and if many cells are in close proximity. The examples shown in Fig. 9c) illustrate the effects to-be-expected. The analytic MCM was used to predict the generated sound pressure at 4 cm distance for a single cell with 40 µm radius. In addition, two honeycomb elements, one with 7 and the other with 19 cells are shown. Both elements exhibit a cell-to-cell distance of 88 µm. For the 7-cell element, the sound pressure scales up, and only a small shift in f_{pk} occurs. The 19-cell element exhibits higher pressures at higher frequencies, with a shift in f_{pk} and an additional peak. Hence, mutual acoustic impedance effects become stronger with an increasing number of cells.

This work is licensed under a Creative Commons Attribution-NonCommercial-NoDerivatives 4.0 License. For more information, see https://creativecommons.org/licenses/by-nc-nd/4.0/

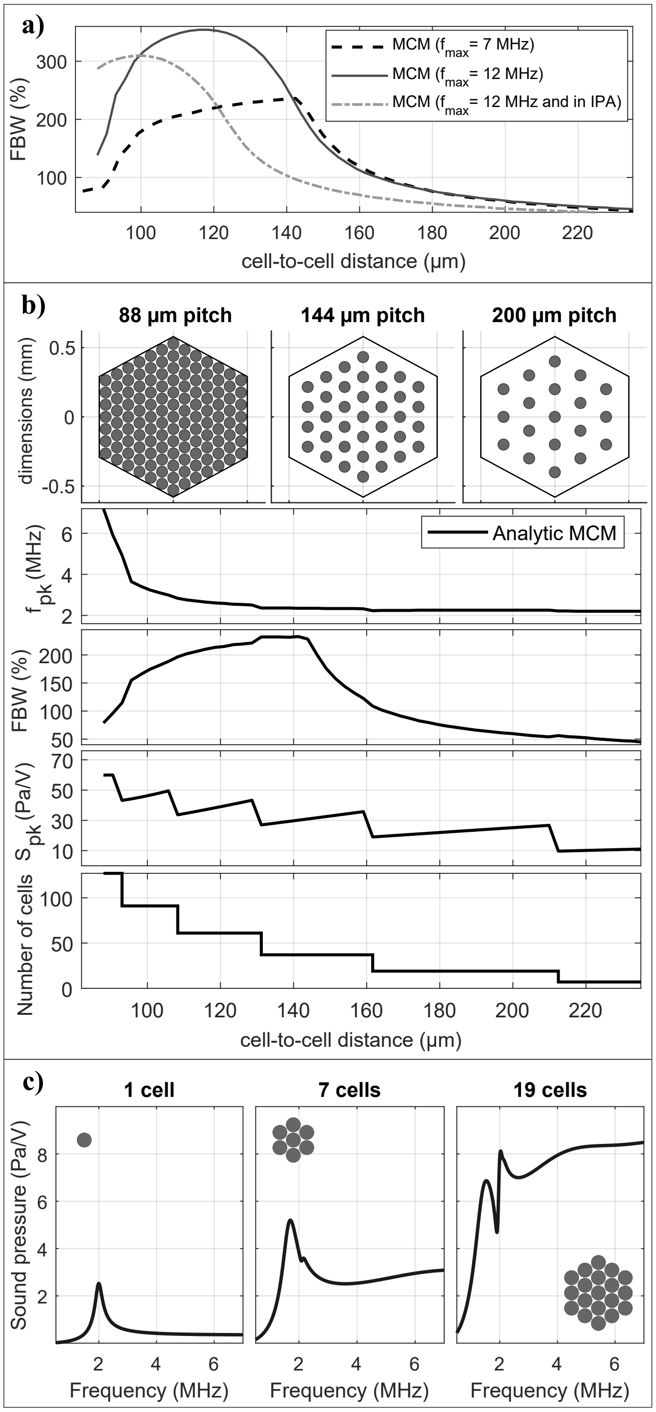

FIGURE 9. **Investigating the effects of mutual acoustic impedance with the analytic MCM on different design aspects and parameters. (a) Changes in FBW when increasing the frequency range of the MCM from 7 MHz to 12 MHz and when replacing water with IPA. (b) Effects when keeping the element size constant: The upper graphs show three exemplary elements with increasing pitches and varying number of cells (limited by the constant element size). The lower graphs give the changes in acoustic characteristics and the number of cells for the respective elements. (c) Modeled transmit sound pressures in water at 4 cm axial distance for a single cell and two honeycomb elements consisting of 7 and 19 cells in close proximity. The grey dots show the arrangements of the cells.**

CMUT elements intended for linear arrays typically feature a rectangular shape with only a few columns of cells and a larger number of rows [16, 20]. Hence, acoustic cross-coupling is lower in lateral direction than in elevation direction. This differs for transducer array designs, where symmetric acoustic fields are required, such as 2-D matrix arrays [42] or sparse arrays for 3-D ultrasound tomography [6]. In the latter case, state-of-the art full wave inversion reconstruction algorithms require transducers with frequency components below 1 MHz [5]. Hence, acoustic cross-coupling effects between cells have to be considered in the design process to meet the required acoustic fields.

Since the analytic definition of the mutual acoustic impedance in (7) depends only on the radius of the cells and their distances, the presented results are also valid for other transducer technologies such as piezoelectric MUTs, if multiple radiators are driven in parallel. Though for this case, the definition of the cell would need to be adapted to match the respective technology.

Though both models capture the general effects, a significant mismatch remains with the measurements, especially in terms of S_{pk} and FBW. The analytic MCM overestimates the peaking in sound pressure, evident in the predictions for the 220 μm design. The peak at around 2.5 MHz in the 132 μm predictions (see Fig. 7c)) arises from the increase in mutual radiation resistance, which seems to be less prominent in real life. The FE model aligns more closely with the measurements, though an overestimation of the sound pressure for larger pitches (176 μm and 220 μm) can be observed. However, the difference in absolute pressure might also arise from performance variations of the produced samples. A larger measurement series is required to gather more data in this respect in order to obtain the mean performance.

Prominent changes in the acoustic fields were observed in the measured samples, emphasizing the need for accurate simulations of entire elements. Despite the mismatch between the analytic MCM and measurements, the low computational costs and the capability to directly predict the acoustic far-field make it a valuable tool in the design process. The model can be applied to get fast design ideas and to identify suitable parameter combinations and their expected impact on the acoustic performance. However, when interpreting the results, it is important to be aware of its limitations (overestimation in sound pressure, S_{pk} and FBW). Once a suitable design is found, a FE simulation should be performed with this parameter set and the results compared with measurements. The rapid production cycles of polyCMUTs offer an ideal environment for design validations, enabling the fast identification of differences and iterative improvements.

In future work, we want to improve both models to better fit the measurements. For the FE model, an adjustment of the mechanical boundary conditions, e.g. by removing fixed boundaries, and including realistic damping properties for

This work is licensed under a Creative Commons Attribution-NonCommercial-NoDerivatives 4.0 License. For more information, see https://creativecommons.org/licenses/by-nc-nd/4.0/

This article has been accepted for publication in IEEE Open Journal of Ultrasonics, Ferroelectrics, and Frequency Control. This is the author's version which has not been fully edited and content may change prior to final publication. Citation information: DOI 10.1109/OJUFFC.2024.3371913

the polymeric materials could improve predictions. For the analytic MCM, the lumped components modeling a single-cell can be refined to better cover the behavior. An interesting approach in this respect was presented by Savoia et. al [43]. In this work, results from FE simulations were incorporated in an equivalent circuit model to more realistically represent the vibration behavior of CMUTs. Further aspects to improve the model predictions are to consider damping effects as well as the limited conductivity of thin metal layers and parasitic capacitances. In the latter case, a phase delay between the cells can be introduced by adding a distributed capacitor-resistor network to the equivalent circuit model. This will affect the acoustic cross-coupling between cells and consequently, the macroscopic acoustic field.

VI. CONCLUSION

In this work, we investigated changes in ultrasound characteristics of transducers consisting of multiple radiators when varying the cell-to-cell spacing. As a practical example we studied hexagonal, polymer-based CMUT elements using analytic and finite element models. In addition, we fabricated several prototypes for evaluation and comparison, giving detailed explanations on novel fabrication processes.

We found a strong dependence of acoustic characteristics on the cell spacing. The primary cause of this dependence was found to be mutual acoustic impedance effects between the cells. For densely packed, rotational symmetric elements, the peak frequency is shifted significantly to higher frequencies, compared to the performance of a single cell. With increasing cell spacing, the element's peak frequency converges towards that of a single cell. In addition, a gradual increase in peak sensitivity occurs. The fractional bandwidth of the element is affected as well, with an analytically predicted maximum at approx. 1.7 times the cell diameter for the investigated designs within a defined frequency range.

The results of this work show that effects introduced by acoustic cross-coupling between cells need to be considered to match transducer design goals accurately. This is of special importance for element designs where a dense 3-D arrangement of cell are required. For applications which aim for a large bandwidth, a small to intermediate cell spacing should be foreseen. Applications which require a high output pressure in a limited frequency range, a larger cell spacing may lead to a better performance. Future work will focus on exploring these effects in more detail. Our goal is to derive design rules to achieve optimal performance of polyCMUTs in terms of bandwidth and sensitivity. This encompasses different element shapes, cell arrangements and frequency ranges.

ACKNOWLEDGMENTS

We acknowledge the support of the Government of Canada's New Frontiers in Research Fund (NFRF), NFRFT-2020-00238. The fabrication costs were supplemented by CMC Microsystems MNT Award 10869. The authors thank CMC Microsystems, UBC AMPEL Nanofab and the UBC Bioimaging Facility for their kind support. The authors declare the following financial interests / personal relationships which may be considered as potential competing interests: Gerardo, Cretu and Rohling are founders and directors of Sonus Microsystems, and Rohling is a founder and executive of Sonic Incytes.

References

[1] T. R. Gururaja and R. K. Panda, "Current status and future trends in ultrasonic transducers for medical imaging applications," in *Proceedings of the 11th IEEE Symposium on Applications of Ferroelectrics*, 1998.

[2] A. Safari, V. F. Janas, and A. Bandyopadhyay, "Development of fine-scale piezoelectric composites for transducers," *AIChE Journal*, vol. 43, no. 11, pp. 2849–2856, 1997.

[3] W. Lee and Y. Roh, "Ultrasonic transducers for medical diagnostic imaging," *Biomedical Engineering Letters*, vol. 7, no. 2, pp. 91–97, 2017.

[4] S. Cochran, "Piezoelectricity and basic configurations for piezoelectric ultrasonic transducers," in *Ultrasonic Transducers*, K. Nakamura, Ed. Cambridge, UK: Woodhead Publishing Limited, 2012, ch. 1, pp. 3–35.

[5] M. Roberts, E. Martin, M. D. Brown, B. T. Cox, and B. E. Treeby, "Open-UST: An open-source ultrasound tomography transducer array system," *IEEE Transactions on Ultrasonics, Ferroelectrics, and Frequency Control*, vol. 70, no. 7, pp. 782–791, 2023.

[6] M. Angerer, M. Zapf, S. Gebhardt, H. Neubert, and N. V. Ruiter, "Single-fiber transducer arrays for 3D ultrasound computed tomography: From requirements to results," *IEEE Transactions on Ultrasonics, Ferroelectrics, and Frequency Control*, vol. 70, no. 7, pp. 772–781, 2023.

[7] I. Wygant, "A comparison of CMUTs and piezoelectric transducer elements for 2D medical imaging based on conventional simulation models," in *2011 IEEE International Ultrasonics Symposium (IUS)*, 2011.

[8] A. S. Savoia, G. Caliano, and M. Pappalardo, "A CMUT probe for medical ultrasonography: From microfabrication to system integration," *IEEE Transactions on Ultrasonics, Ferroelectrics, and Frequency Control*, vol. 59, no. 6, pp. 1127–1138, 2012.

[9] E. B. Dew, A. Kashani Ilkhechi, M. Maadi, N. J. M. Haven, and R. J. Zemp, "Outperforming piezoelectric ultrasonics with high-reliability single-membrane CMUT array elements," *Microsystems and Nanoengineering*, vol. 8, no. 59, 2022.

[10] J. Joseph, B. Ma, and B. T. Khuri-Yakub, "Applications of capacitive micromachined ultrasonic transducers: A comprehensive review," *IEEE Transactions on Ultrasonics, Ferroelectrics, and Frequency Control*, vol. 69, no. 2, pp. 456–467, 2022.

This work is licensed under a Creative Commons Attribution-NonCommercial-NoDerivatives 4.0 License. For more information, see https://creativecommons.org/licenses/by-nc-nd/4.0/

This article has been accepted for publication in IEEE Open Journal of Ultrasonics, Ferroelectrics, and Frequency Control. This is the author's version which has not been fully edited and content may change prior to final publication. Citation information: DOI 10.1109/OJUFFC.2024.3371913

[11] A. S. Ergun, H. Yongli, Z. Xuefeng, O. Oralkan, G. G. Yarahoglu, and B. T. Khuri-Yakub, “Capacitive micromachined ultrasonic transducers: Fabrication technology,” *IEEE Transactions on Ultrasonics, Ferroelectrics, and Frequency Control*, vol. 52, no. 12, pp. 2242–2258, 2005.

[12] M. S. Salim, M. F. Abd Malek, R. B. W. Heng, K. M. Juni, and N. Sabri, “Capacitive micromachined ultrasonic transducers: Technology and application,” *Journal of Medical Ultrasound*, vol. 20, no. 1, pp. 8–31, 2012.

[13] R. L. Pritchard, “Mutual acoustic impedance between radiators in an infinite rigid plane,” *The Journal of the Acoustical Society of America*, vol. 32, no. 6, pp. 730–737, 1960.

[14] D. T. Porter, “Self- and mutual-radiation impedance and beam patterns for flexural disks in a rigid plane,” *The Journal of the Acoustical Society of America*, vol. 36, no. 6, pp. 1154–1161, 1964.

[15] A. Caronti, A. Savoia, G. Caliano, and M. Pappalardo, “Acoustic coupling in capacitive microfabricated ultrasonic transducers: Modeling and experiments,” *IEEE Transactions on Ultrasonics, Ferroelectrics, and Frequency Control*, vol. 52, no. 12, pp. 2220–2234, 2005.

[16] A. Caronti *et al.*, “Capacitive micromachined ultrasonic transducer (CMUT) arrays for medical imaging,” *Microelectronics Journal*, vol. 37, no. 8, pp. 770–777, 2006.

[17] M. N. Senlik, S. Olcum, H. Koymen, and A. Atalar, “Radiation impedance of an array of circular capacitive micromachined ultrasonic transducers,” *IEEE Transactions on Ultrasonics, Ferroelectrics, and Frequency Control*, vol. 57, no. 4, pp. 969–976, 2010.

[18] H. K. Oguz, A. Atalar, and H. Köymen, “Equivalent circuit-based analysis of CMUT cell dynamics in arrays,” *IEEE Transactions on Ultrasonics, Ferroelectrics, and Frequency Control*, vol. 60, no. 5, pp. 1016–1024, 2013.

[19] M. Maadi and R. J. Zemp, “Self and mutual radiation impedances for modeling of multi-frequency CMUT arrays,” *IEEE Transactions on Ultrasonics, Ferroelectrics, and Frequency Control*, vol. 63, no. 9, pp. 1441–1454, 2016.

[20] T. Merrien, A. Boulmé, and D. Certon, “Lumped-parameter equivalent circuit modeling of CMUT array elements,” *IEEE Open Journal of Ultrasonics, Ferroelectrics, and Frequency Control*, vol. 2, pp. 1–16, 2022.

[21] A. Boulmé, D. Certon, N. Sénégond, C. Meynier, and F. Teston, “A strategy to predict and reduce baffle effects in linear array of CMUTs,” in *2010 IEEE International Ultrasonics Symposium (IUS)*, 2010.

[22] M. Angerer, J. Welsch, C. D. Gerardo, N. V. Ruiter, E. Cretu, and R. Rohling, “Exploring the potentials of polymer-based CMUTs for 3D ultrasound computed tomography,” in *2023 IEEE International Ultrasonics Symposium (IUS)*, 2023.

[23] H. Gemmeke *et al.*, “The new generation of the KIT 3D USCT,” in *1st International Workshop on Medical Ultrasound Tomography*, KIT Scientific Publishing, 2018.

[24] C. D. Gerardo, E. Cretu, and R. Rohling, “Fabrication and testing of polymer-based capacitive micromachined ultrasound transducers for medical imaging,” *Microsystems and Nanoengineering*, vol. 4, no. 1, 2018.

[25] M. Angerer, M. Zapf, S. Gebhardt, H. Neubert, and N. V. Ruiter, “Enhanced KLM model for single-fibre piezocomposite transducers,” in *2023 IEEE International Ultrasonics Symposium (IUS)*, 2023.

[26] M. Angerer, *Transducer Arrays for 3D Ultrasound Computed Tomography*. PhD thesis, Karlsruhe Institute of Technology, KIT scientific publishing, 2022.

[27] W. P. Mason, *Electromechanical transducers and wave filters*. London: Van Nostrand, 1948.

[28] F. V. Hunt, *Electroacoustics: The analysis of transduction, and its historical background*. American Institute of Physics, 1982.

[29] S. G. Ergun, G. G. Yaralioglu, and P. Khuri-Yakub, “Capacitive micromachined ultrasonic transducers: Theory and technology,” *Journal of Aerospace Engineering - J AEROSP ENG*, vol. 16, no. 2, 2003.

[30] A. Lohfink and P. Eccardt, “Linear and nonlinear equivalent circuit modeling of CMUTs,” *IEEE Transactions on Ultrasonics, Ferroelectrics, and Frequency Control*, vol. 52, no. 12, pp. 2163–2172, 2005.

[31] I. O. Wygant, M. Kupnik, and B. T. Khuri-Yakub, “Analytically calculating membrane displacement and the equivalent circuit model of a circular CMUT cell,” in *IEEE Ultrasonics Symposium*, 2008.

[32] D. Horsley, Y. Lu, and O. Rozen, “Flexural piezoelectric resonators,” in Springer International Publishing, 2017, pp. 153–173.

[33] M. Greenspan, “Piston radiator: Some extensions of the theory,” *The Journal of the Acoustical Society of America*, vol. 65, no. 3, pp. 608–621, 1979.

[34] K. K. Park, M. Kupnik, H. J. Lee, B. T. Khuri-Yakub, and I. O. Wygant, “Modeling and measuring the effects of mutual impedance on multi-cell CMUT configurations,” in *2010 IEEE International Ultrasonics Symposium*, 2010.

[35] A. Omidvar, E. Cretu, R. Rohling, M. Cresswell, and A. J. Hodgson, “Flexible polyCMUTs: Fabrication and characterization of a flexible polymer-based capacitive micromachined ultrasonic array for conformal ultrasonography,” *Advanced Materials Technologies*, vol. 8, no. 5, p. 2 201 316, 2023.

[36] E. L. Kinsler, *Fundamentals of Acoustics*, 4th. John Wiley and Sons, 2000, pp. 188–191.

This work is licensed under a Creative Commons Attribution-NonCommercial-NoDerivatives 4.0 License. For more information, see https://creativecommons.org/licenses/by-nc-nd/4.0/

This article has been accepted for publication in IEEE Open Journal of Ultrasonics, Ferroelectrics, and Frequency Control. This is the author's version which has not been fully edited and content may change prior to final publication. Citation information: DOI 10.1109/OJUFFC.2024.3371913

[37] J. Welsch, E. Cretu, R. Rohling, and C. D. Gerardo, "Ultrathin, high sensitivity polymer-based capacitive micromachined ultrasound transducers (polyCMUTs) for acoustic emission sensing in fiber reinforced polymers," in *2022 IEEE International Ultrasonics Symposium (IUS)*, 2022.

[38] pan-European MEMS ultrasound transducer consortium, "A european MEMS ultrasound benchmark," ECSEL Joint Undertaking project POSITION-2, Report, 2021.

[39] A. Atalar, H. Köymen, and H. K. Oğuz, "Rayleigh–bloch waves in CMUT arrays," *IEEE Transactions on Ultrasonics, Ferroelectrics, and Frequency Control*, vol. 61, no. 12, pp. 2139–2148, 2014.

[40] O. Oralkan, S. T. Hansen, B. Bayram, G. G. Yaralioglu, A. S. Ergun, and B. T. Khuri-Yakub, "High-frequency CMUT arrays for high-resolution medical imaging," in *2004 IEEE International Ultrasonics Symposium (IUS)*, 2004.

[41] Z. Izadifar, Z. Izadifar, D. Chapman, and P. Babyn, "An introduction to high intensity focused ultrasound: Systematic review on principles, devices, and clinical applications," *Journal of Clinical Medicine*, vol. 9, no. 2, p. 460, 2020.

[42] O. Oralkan *et al.*, "Volumetric ultrasound imaging using 2-D CMUT arrays," *IEEE Transactions on Ultrasonics, Ferroelectrics, and Frequency Control*, vol. 50, no. 11, pp. 1581–1594, 2003.

[43] A. S. Savoia, G. Scaglione, and B. Haider, "Combined use of finite element and equivalent circuit modeling for system-level simulation of integrated capacitive micromachined ultrasonic transducers (CMUT)," in *2020 IEEE International Ultrasonics Symposium (IUS)*, 2020.

MARTIN ANGERER (Member, IEEE) received the B.Eng. degree in Mechatronics from the Munich University of Applied Sciences, Germany, in 2012, the M.Sc. degree in Medical Engineering Science from the University of Lübeck, Germany, in 2014, and the Ph.D. degree in Electrical Engineering and Information Technology from the Karlsruhe Institute of Technology (KIT), Germany, in 2022. From 2015 to 2018, he was a Development Engineer with MED-EL Medical Electronics, Innsbruck, Austria, working on acoustic sensors for fully-implantable cochlear implants. He is currently a Postdoctoral Fellow with the University of British Columbia in Vancouver, Canada.

Dr. Angerers research interests lie in the field of novel sensors and transducers, with a focus on medical applications. His expertise encompasses the development, modeling, fabrication, characterization, and optimization of piezoelectric and MEMS-based technologies.

JONAS WELSCH received his B. Sc. In Aerospace Engineering at the University of Stuttgart in 2017. During his Masters he worked as a process optimization engineer at an SME in Germany, acquiring skills in project management, lean manufacturing and fabrication process planning. He received his M. Sc. in Aerospace Engineering in 2019 with a focus on space craft design and materials engineering, specifically composites. During his master thesis on polymer based capacitive micromachined ultrasound transducers for structural health monitoring at the University of British Columbia he discovered his interest in sensing technologies for non-destructive testing and a love for all things microfabrication. He joined Prof.'s E. Cretu and R. Rohling for a PhD at the University of British Columbia and continues his research in the field. His efforts have led to being awarded the best paper award at the IEEE International Ultrasonic Symposium in Venice in 2022.

CARLOS D. GERARDO received his B.Sc. degree in Electromechanical Engineering and his M.Sc. degree in Electrical Engineering from the Autonomous University of San Luis Potosi, SLP, Mexico. From 2010 until 2012 he worked an Electrical Design Engineer at the General Electric Company in Santiago de Queretaro, Mexico. He got his PhD in Electrical and Computer Engineering from The University of British Columbia in 2018, where he helped to develop the polyCMUT technology. He kept working as a Postdoctoral Researcher in the same institution from 2019 to 2023 to keep improving the technology. His research focuses on the design, simulation, fabrication and characterization of MEMS ultrasound devices.

NICOLE V. RUITER received the M.Sc. degree in Medical Informatics (Dipl. Inform. Med.) from Ruprechts University Heidelberg, Germany. She has a Ph.D. degree in Informatics (Dr. rer. nat.) from University of Mannheim, Germany and 'Habilitation' at Karlsruhe Institute of Technology, Germany. She is a senior researcher at the Institute for Data Processing and Electronics at Karlsruhe Institute of Technology. Her research interests include 3-D ultrasound tomography, medical image reconstruction, multimodal registration and biomechanical modeling. She has authored more than 100 papers in international journals and conferences.

EDMOND CRETU (Member, IEEE) received the Ph.D. degree in electrical engineering from the Delft University of Technology, The Netherlands, in 2003. From 1990 to 1994, he held a Researcher position at the Romanian Academy. From 2000 to 2005, he was a Senior Designer and the Project Manager of Melexis, Belgium. Since 2006, he has been with the Department of Electrical and Computer Engineering, The University of British Columbia, where he is currently a Professor. His research areas are related to MEMS/NEMS, signal processing and control, microsystems, and sensor networks.

This work is licensed under a Creative Commons Attribution-NonCommercial-NoDerivatives 4.0 License. For more information, see https://creativecommons.org/licenses/by-nc-nd/4.0/

This article has been accepted for publication in IEEE Open Journal of Ultrasonics, Ferroelectrics, and Frequency Control. This is the author's version which has not been fully edited and content may change prior to final publication. Citation information: DOI 10.1109/OJUFFC.2024.3371913

ROBERT ROHLING (Fellow, IEEE) received the Ph.D. degree in information engineering from the University of Cambridge, Cambridge, U.K., in 1998. He is currently a Professor at The University of British Columbia (UBC), Vancouver, BC, Canada, with appointments in electrical and computer engineering and mechanical engineering. After his Ph.D. degree, he developed 3-D medical imaging software in industry before starting a faculty position at UBC in 2001. He is also the Director of the Institute for Computing, Information and Cognitive Systems, UBC, where 150 faculty members are engaged in multidisciplinary research. His work spans medical imaging with a focus on ultrasound, image-guided interventions, and tissue characterization. He holds 16 granted patents and has founded two start-ups.

This work is licensed under a Creative Commons Attribution-NonCommercial-NoDerivatives 4.0 License. For more information, see https://creativecommons.org/licenses/by-nc-nd/4.0/